

Ferrimagnetism in sputtered Mn_xCoGe thin films

D. Kalliecharan,¹ J. S. R. McCoombs,¹ M. M. E. Cormier,¹ B. D. MacNeil,¹ R. L. C. Molino,¹ and T. L. Monchesky^{1,*}

¹*Department of Physics and Atmospheric Science,
Dalhousie University, Halifax, Nova Scotia, Canada B3H 3J5*

(Dated: October 2, 2019)

Investigations into the magnetic properties of sputtered Mn_xCoGe films in the range $0.8 \leq x \leq 2.5$ uncovered ferrimagnetic order, unlike the ferromagnetic order reported in bulk samples. These films formed hexagonal Ni_2In -type structures in all measured compositions. While the Curie temperatures of the films are comparable to those of hexagonal bulk MnCoGe , there is a reduction in the magnetization of the Mn_xCoGe film relative to bulk MnCoGe , and a magnetization compensation point is observed in the $x < 1$ samples. To understand the behavior, we calculated the magnetic moments of Mn-antisite defects in MnCoGe with density-function theory calculations. Models constructed from the calculation suggest that films become ferrimagnetic due to the presence of Mn on the Co and Ge sites. In the $x < 1$ samples, these defects arose from the disorder in the films, whereas for $x > 1$, the excess Mn was driven onto the antisites and produced ferrimagnetic order.

I. INTRODUCTION

The manganese germanides provide a rich phase diagram with a diverse range of magnetic structures. Mn_3Ge forms one of two polytypes. The Mn_3Ge D0_{19} hexagonal structure is a frustrated non-collinear antiferromagnet with a large topological Hall effect¹, while the tetragonal D0_{22} Heusler is a high-anisotropy ferrimagnet of interest for memory applications². There have been recent proposals for tuning the magnetic properties of this structure via chemical substitutions $\text{Mn}_{3-y}\text{X}_y\text{Ge}$.³ Substitution of Ni, for example, decreases the moment and increases the coercivity.⁴

A related family of compounds – the inverse tetragonal Heuslers – is obtained by replacing Mn on one of the 4d Wyckoff sites in the D0_{22} structure, $(0, 1/2, 1/4)$, with another element. This lowers the symmetry from D_{3h} to the non-centrosymmetric D_{2d} point group and turns on the Dzyaloshinskii-Moriya interaction that is responsible for the non-collinear magnetic structures in Mn_2RhSn ⁵ and $\text{Mn}_{1.4}\text{PtSn}$ ⁶. The stability of the Mn_2XGe Heusler compounds have been explored by density-functional theory (DFT) calculations,⁷ many of which are predicted to form the inverse tetragonal structure, including Mn_2CoGe . The initial motivation for the work in this paper was to create Mn_2CoGe Heusler alloy films by magnetron sputtering. We fabricated Mn_xCoGe in the compositional range $0.8 \leq x \leq 2.5$, but were unsuccessful in producing Heusler alloys. The entire composition formed either a hexagonal structure or an orthorhombic structure related to the magnetocaloric material, MnCoGe .

At low temperature, MnCoGe forms an orthorhombic C23 TiNiSi -type structure (space group #62, $Pnma$). It is a collinear ferromagnet with a Curie temperature, $T_C^{\text{ortho}} = 355$ K and a magnetic moment of $m = 3.86\mu_B/\text{formula unit}$ (f.u.). At a temperature T_t , the material undergoes a martensitic transformation to a hexagonal B8_2 Ni_2In -type structure (space group #194 $P6_3/mmc$).⁸ The resulting 3.9% contraction in volume

leads to a broadening of the Mn d-bands producing a smaller moment and lower T_C ⁹. In this hexagonal polytype, $m = 2.78\mu_B/\text{f.u.}$ ¹⁰ and $T_C^{\text{hex}} \approx 260$ K. The martensitic transition is very sensitive to defects. Johnson *et al.* found that T_t varied between 398 – 453 K, while Kanomata *et al.* reported T_t as high as 650 K. When T_t lies between T_C^{hex} and T_C^{ortho} the material undergoes a first-order transition from an orthogonal ferromagnet, to a hexagonal paramagnet that gives rise to a large magnetocaloric effect.

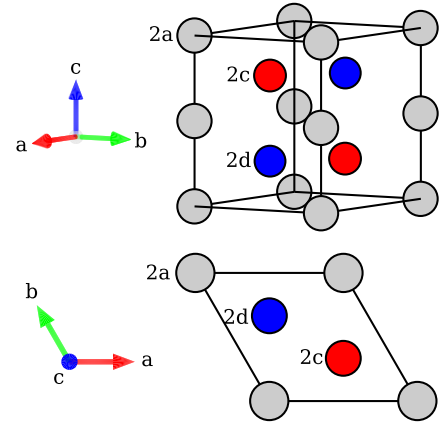


FIG. 1. The primitive unit cell of MnCoGe Ni_2In -type phase. Isometric view (top) and c-axis projection (bottom), showing the 2a-Mn sites (gray), the 2c-Co sites (red) and 2d-Ge sites (blue).

What makes MnCoGe particularly attractive is that its martensitic temperature can be chemically tuned independent of T_C . The transition temperature T_t is very sensitive to Co vacancies,^{11,12} as well as Mn vacancies.¹³ With only a few percent vacancies on either site, T_t can be reduced to room temperature with little effect on either T_C^{hex} or T_C^{ortho} . This is potentially driven by a reduction in the number of valence electrons, as the same effect is also observed in $\text{Mn}_{1+x}\text{Co}_{1-x}\text{Ge}$ alloys.^{13,14} Numerous studies have explored the influence of other defects and

substitutions in MnCoGe; a comprehensive summary of such studies is given in the appendix of Ref. 15.

In the Ni₂In-phase, Mn resides on the 2a (0,0,0) Wyckoff sites and forms low density (001) planes. These are separated by dense CoGe planes with Co on the 2c (1/3, 2/3, 1/4) sites and Ge on the 2d (2/3, 1/3, 1/4) sites (see Fig. 1).

We found that Mn_xCoGe films prepared by DC magnetron sputtering were much more disordered than typical bulk material, which had two important consequences. Firstly, the hexagonal B8₂ phase was obtained at room temperature after annealing at $T = 500$ °C and remained in this phase upon cycling down to low temperature, consistent with other reports of sputtered MnCoGe films.¹⁶ Secondly, the films display ferrimagnetic rather than ferromagnetic order reported in other investigations of this material. We support the analysis of the magnetic properties with DFT calculations that show the spins from Mn-antisite defects align in the opposite direction to the spins on the Mn-sites.

II. GROWTH

Films were deposited on thermally oxidized wafers, as SiO₂ acts as a diffusion barrier for Mn, Co and Ge¹⁷. Si(001) wafers (manufactured by *Prolog semicor Ltd.*) were cut into 20 mm × 20 mm squares and were sonicated in acetone and methanol baths for 15 minutes each. Before removing the wafers from the methanol bath, de-ionized nanopure water was slowly added and allowed to overflow in order to remove any contaminants from the liquid surface. The wafers were heated in a dry furnace at 900 °C for 5 hours to create a SiO₂ layer, approximately 300 nm in thickness.

The sonication treatment was then repeated prior to loading samples into a *Corona Vacuum Coater V3T* magnetron sputtering deposition system with a base pressure of 3.0×10^{-7} Torr. The Ar pressure during sputtering was 2.0×10^{-3} Torr. Sputtering rates were calibrated by measuring the weights of the samples before and after growth. The compositions were verified using a *Thermo iCAP Q* laser ablation inductively coupled plasma mass spectrometer (LA-ICP-MS). The results are shown in Table I.

The as-grown amorphous films were crystallized *ex-situ* by annealing in an Ar environment in a *Modular Process Technology RTP600s* Rapid Thermal Annealer (RTA). The RTA reached the desired temperatures within 20 s (15–35 °C/s), and were cooled at a rate of approximately 2 °C/s.

III. STRUCTURAL CHARACTERIZATION

The crystal structures of the films were investigated with conventional X-ray diffraction (XRD) $\theta - 2\theta$ measurements on a *Siemens D500 Diffractometer* equipped

with a Cu source and monochromator. To determine the strain in the films, the XRD measurements were compared to grazing angle X-ray diffraction (GAXRD) measurements, where the incident X-ray beam is fixed at $\theta_i = 6^\circ$. The alignment of the diffractometer was checked with a Si powder sample for both the XRD and the GAXRD geometries.

Annealing times and temperatures were selected to produce single phase samples. Five sets of samples – Mn_{0.8}CoGe, Mn_{0.9}Co_{0.8}Ge, Mn_{1.4}CoGe, Mn_{1.8}Co_{0.8}Ge and Mn_{2.5}CoGe – were annealed within the temperature range of 375 °C - 500 °C for an interval time between 2 minutes and 40 minutes, yielding Ni₂In-type polycrystalline films. High temperature annealing resulted in mixed phase samples: annealing at 700 °C produced a mixture of Ni₂In-type and TiNiSi-type phases, but there was no evidence of a tetragonal phase. Figure 2 shows fits to GAXRD measurements of the Ni₂In-type samples that demonstrate the phase is stable across the entire composition range, $0.8 \leq x \leq 2.5$.

The lattice parameters extracted from the GAXRD fits (Table I), are comparable to the values of bulk MnCoGe, $a = 4.087(1)$, $c = 5.316(3)$ Å.¹⁸ The Rietveld refinements were performed using Rietica version 4.0 (<http://rietica.org>). We note that the (101) peak intensity is much lower than expected from bulk MnCoGe samples. The discrepancy could be accounted for with 20% vacancies on the 2c-site occupied by Co. The presence of vacancies is consistent with ICP-MS measurements that show Mn concentrations are lower than the nominal value. The intensity of the (2 $\bar{1}$ 0)-peaks is higher than expected. As the annealing process can lead to preferred grain orientation, it is not possible to separate this effect from the possibility of vacancies.

TABLE I. The composition of the Mn_xCoGe films determined by LA-ICP-MS, together with lattice parameters determined from GAXRD.

x	$\chi_{\text{Mn}}/\chi_{\text{Ge}}$	$\chi_{\text{Co}}/\chi_{\text{Ge}}$	a (Å)	c (Å)
0.8	0.79	0.93	4.02	5.21
0.9	0.89	0.79	4.03	5.23
1.4	1.42	0.97	4.05	5.30
1.8	1.83	0.78	4.05	5.36
2.5	2.47	1.07	4.07	5.29

The GAXRD peak positions were found to be systematically lower than the XRD measurements (unlike the control Si powder sample). A comparison between GAXRD and XRD is shown in Fig. 3(a). While XRD probes the lattice parameters of planes that are parallel to the substrate surface, GAXRD measures interatomic planes whose normal is further and further from the film normal as the detector angle θ increases. We define $\phi = \theta - \theta_i$ as the angle between this normal and the film's normal. As shown below, the shift in the GAXRD peaks relative to those in the conventional XRD measurements is due to strain in the films. To determine the influence of film strain on the GAXRD measurements, we assume

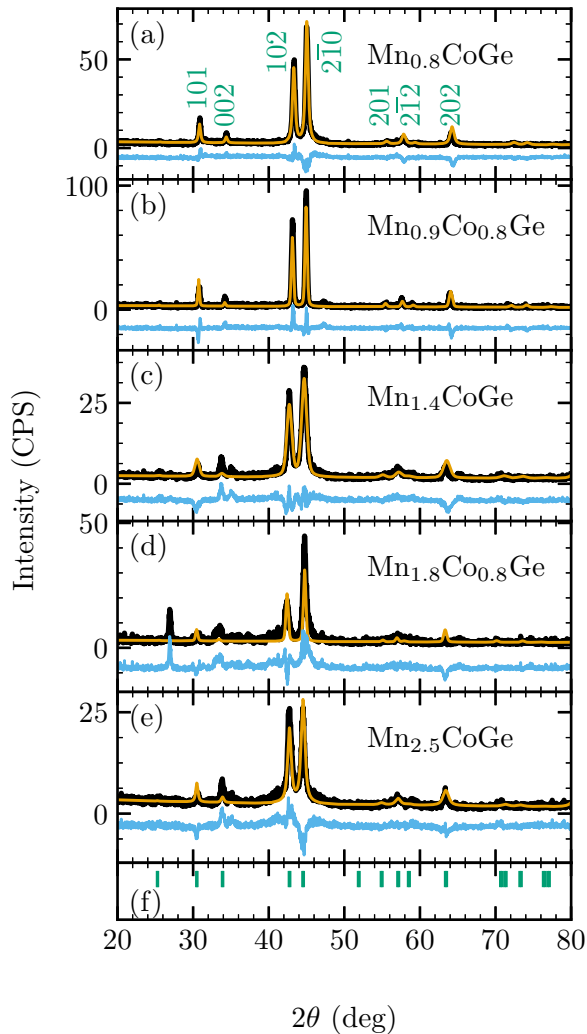


FIG. 2. XRD data (black) with Reitveld refinements (orange), residuals (blue) and Ni_2In -type peak locations (green): (a) $\text{Mn}_{0.8}\text{CoGe}$, (b) $\text{Mn}_{0.9}\text{Co}_{0.8}\text{Ge}$, (c) $\text{Mn}_{1.4}\text{CoGe}$, (d) $\text{Mn}_{1.8}\text{Co}_{0.8}\text{Ge}$ and (e) $\text{Mn}_{2.5}\text{CoGe}$, with hexagonal (green) peak locations in (f).

a uniform biaxial strain of the polycrystalline material, where ϵ_{\perp} and ϵ_{\parallel} are the out-of-plane and in-plane strains in the film, respectively. We obtain an expression for the atomic plane spacing, $d(\phi)$ for planes that are at an angle ϕ with respect to the film surface,

$$\frac{d(\phi)}{d(0)} = \left(\frac{1 + 2\epsilon_{\parallel} \sin^2 \phi + 2\epsilon_{\perp} \cos^2 \phi}{1 + 2\epsilon_{\perp}} \right)^{\frac{1}{2}}, \quad (1)$$

in terms of the plane spacing measured by XRD, $d(0)$.

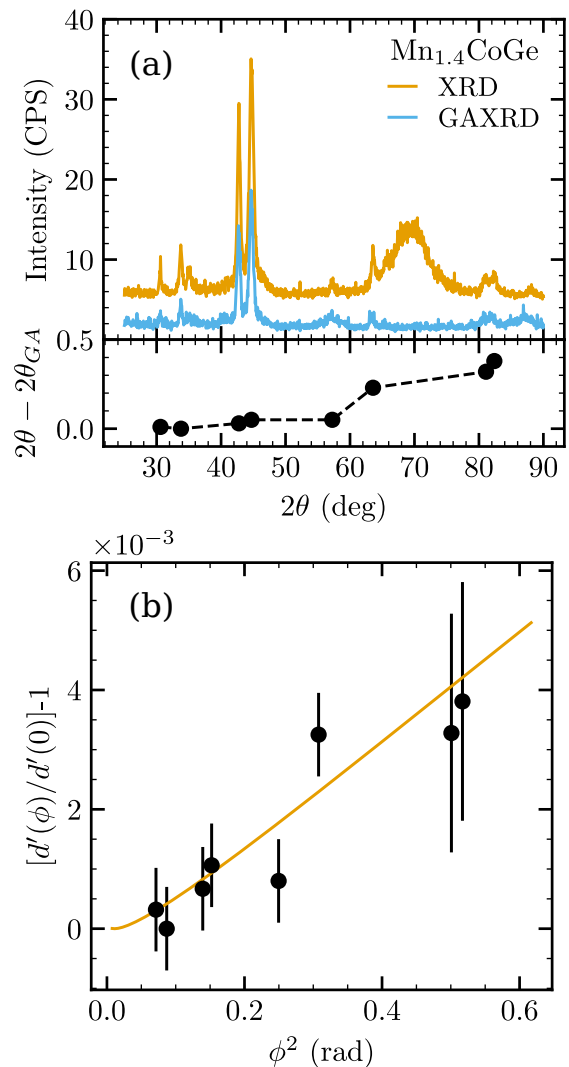


FIG. 3. (a) XRD and GAXRD measurements of $\text{Mn}_{1.4}\text{CoGe}$. The lower panel shows the XRD peak positions relative to GAXRD peaks. Note that in order to be able to see the (202) peak in the XRD data, the intensity of the Si(004) peak at $2\theta = 69.9$ was reduced by offsetting the sample angle by 2° . (b) The normalized change in the interatomic plane spacing as a function of the angle the planes make with the film surface. The solid line show the fit to the data using Eq. (1).

For small strain and small ϕ , $d(\phi) \approx d(0)(\epsilon_{\parallel} - \epsilon_{\perp})\phi^2$. Figure 3b shows a fit to $d(\phi)$ for the $\text{Mn}_{1.4}\text{CoGe}$ sample, which gives $\epsilon_{\parallel} - \epsilon_{\perp} = 0.07 \pm 0.01$.

The strain, which was observed for all Mn_xCoGe films, is likely induced by the annealing process. The thermal expansion coefficients for metals is typically about one order of magnitude larger than the Si substrate. The film crystallizes at high temperature; since the film contracts more than the substrate upon cooling, the film develops an in-plane tensile strain (and through the Poisson ratio, it develops an out-of-plane compressive strain).

IV. MAGNETIC MEASUREMENTS

Magnetic measurements were performed using a *Quantum Design Physical Properties Measurement System* (PPMS), equipped with a *P500 AD/DC Magnetometry System* (ACMS). Samples were cut into 5.8 mm \times 5.8 mm squares and wedged into a plastic straw that was placed in the PPMS. The field was applied in the plane of the film.

Magnetization loops were recorded as the field was cycled between $\mu_0 H = +9$ T and -9 T. The $M - H$ loops for all 5 samples measured at $T = 5$ K are qualitatively similar, as shown in Fig. 4. However, hysteresis loops with $x > 1$ show higher H_C and more rounding, suggestive of a larger mean effective anisotropy with a broader distribution.

The remanent magnetization, M_R , was measured on warming from $T = 5$ K after saturating the film in a 9 T field. The temperature dependence of M_R is shown in Fig. 5. The shape of the $M_R - T$ graph for the $x = 2.5$ sample (shown in yellow) is typical of a ferromagnet. Some of the $x = 2.5$ samples had a small remanent magnetization above $T = 270$ K. Although no impurity phase could be detected in the X-ray measurements, additional annealing in the RTA was able to remove this additional ferromagnetic contribution. The $x = 1.4$ and 1.8 samples also show a small M_R above $T = 270$ K but further annealing could not remove the impurity phase. Unexpectedly, the compositions with $x < 1$ showed ferrimagnetic behavior: above a compensation point of approximately 230 K, the M_R reverses sign.

The Curie temperature is estimated from the temperature where M_R goes to zero. As shown in the Table II, T_C is comparable to the bulk $T_C^{hex} \approx 260$ K of the hexagonal phase, and is relatively insensitive to the composition x , as observed in bulk¹³. However, the table also shows that the total magnetic moment per primitive unit cell is significantly lower than the bulk value for MnCoGe, $5.56\mu_B$ per primitive unit cell.

TABLE II. The saturation magnetization, M_S , the magnetic moment per primitive unit cell, m , the coercive field $\mu_0 H_{ext}$ and Curie Temperature T_C for Mn_xCoGe films.

x	M_S (kA/m)	m (μ_B)	H_C (mT)	T_C (K)
0.8	380	2.99	26	267
0.9	384	3.02	20	260
1.4	497	4.19	78	277
1.8	394	3.19	69	272
2.5	353	2.87	89	267

V. COMPUTED MAGNETIC MOMENTS FROM DENSITY-FUNCTIONAL THEORY

To explore the origin of the drop in magnetic moment and the appearance of ferrimagnetic behavior, we considered the influence of atomic disorder in the Ni_2In struc-

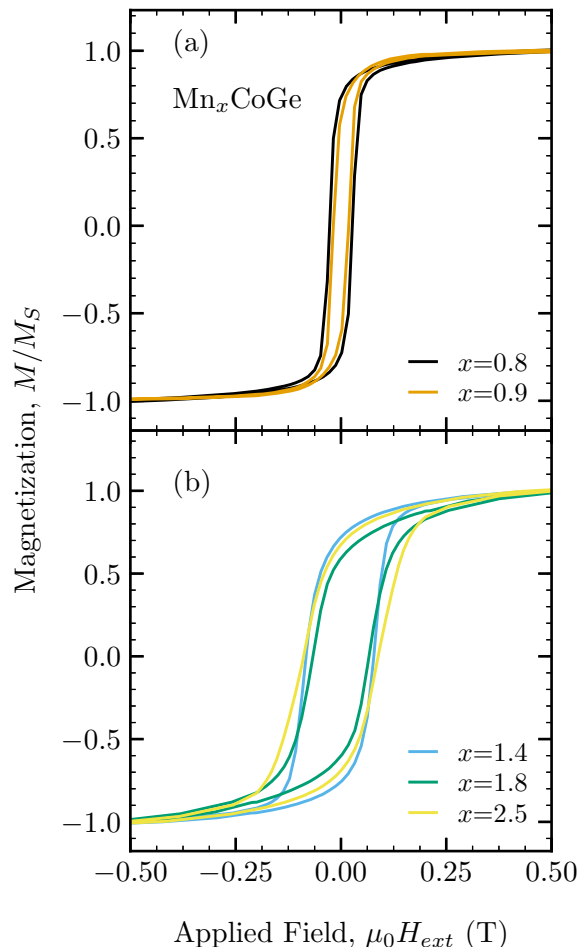


FIG. 4. Normalized hysteresis curves of Mn_xCoGe films for compositions (a) $x < 1$ and (b) $x > 1$. The saturation magnetizations are given in Table II.

ture on the individual magnetic moments. In the ordered phase, nuclear magnetic resonance (NMR) shows that Mn on the 2a-site has a magnetic moment of $m_{Mn} = 2.4 \mu_B$, while the moment of Co on the 2c-site couples ferromagnetically to the 2a-site with a moment $m_{Co} = 0.4 \mu_B$ ¹⁰. These values are in good agreement with the measured magnetization and consistent with neutron scattering experiments¹⁹. However, we note that DFT overestimates the magnetic moment of Mn in $MnCoGe$ ^{9,10,20}, and so has to be rescaled to compare to experiment.

Previously published DFT calculations of Ni_2In -type Mn_2Ge predict ferrimagnetic behavior due to the antiparallel coupling between Mn on 2a- and 2c-sites²¹. This is consistent with tight-binding (TB) calculations for

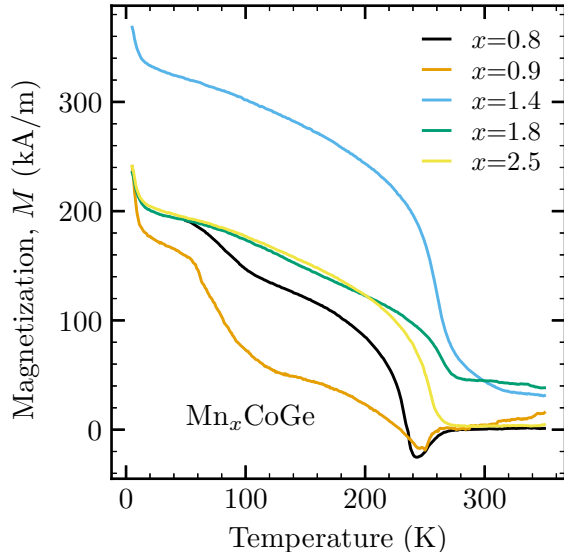


FIG. 5. The nominal structures $\text{Mn}_{0.8}\text{CoGe}$ and $\text{Mn}_{0.9}\text{Co}_{0.8}\text{Ge}$ show ferrimagnetic behaviour due to Mn occupancies on 2a and 2c sites. $\text{Mn}_{1.4}\text{CoGe}$ and $\text{Mn}_{1.8}\text{Co}_{0.8}\text{Ge}$ show a secondary magnetic phase, while the $\text{Mn}_{2.5}\text{CoGe}$ shows a typical M_R -T curve.

MnCoGe that show a reduction in the average Mn moment when it is distributed on both of these sites. The TB calculations show that Co on the other hand is little affected by either moving it to the 2a-site, or by the presence of Mn-antisite defects, as supported by DFT calculations.²² However, there are very few studies of the Ni_2In -type structure and it remains unclear exactly what is the magnetic behavior of Mn on the 2c- and 2d-sites (Mn_{2c} and Mn_{2d}).

DFT^{23,24} computations were performed within the spin-polarized general gradient approximation (GGA)²⁵ using the Vienna Ab-initio Simulation Package (VASP).^{26–29} Local magnetizations are obtained by projecting the ground state crystal orbitals onto atomic-like orbitals centered at each crystallographic site (i.e. atom-centered). Since the magnetization can be strongly dependent on the inter-atomic distances, full cell relaxations were performed for all structures, converging forces to better than $0.01 \text{ eV}/\text{\AA}$ and stresses to within 0.001 GPa by enforcing a sufficiently dense \mathbf{k} -point sampling of the first Brillouin zone. We used projector augmented wave (PAW) datasets with 7, 9, and 4 valence electrons for Mn, Co, and Ge, respectively. The ground state energies were converged to better than 1 meV/f.u. using a plane-wave energy cut-off of 550 eV . We attempted to converge both ferromagnetic and ferrimagnetic solutions for all structures. In some cases both solutions converged, but we present here only the lowest energy solutions.

Our computed magnetic moments for Ni_2In -type MnCoGe and Mn_2Ge agree well with previously calculated values. In MnCoGe , our computations show a slightly smaller Mn moment, $2.75 \mu_B$ compared to the value calculated in Ref. 20 ($3.09 \mu_B$), but one that is closer to the experimental value. We obtain a moment of $0.5 \mu_B$ on Co, and $-0.1 \mu_B$ on Ge that are in good agreement with Ref. 20, as well as experimental values. In Mn_2Ge , our computed magnetizations for Mn_{2a} , $2.9 \mu_B$ and Mn_{2c} , $-2.0 \mu_B$, agree exactly with previously published DFT results.³⁰

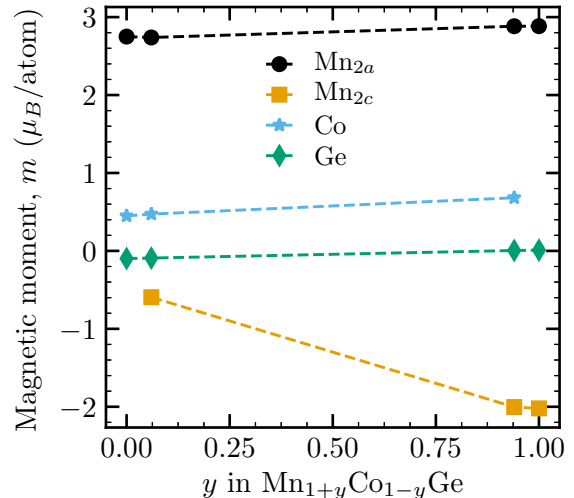


FIG. 6. Magnetic moments as a function of the fraction of Mn on the Co 2c-site (see fig. 5), computed from DFT. A linear approximation to the variation in the Mn_{2c} moment is given by $m_{\text{Mn}_{2c}}(y) = -1.43y - 0.514$.

To determine the effect of Mn_{2c} , $2 \times 2 \times 2$ supercells were built by repeating the MnCoGe hexagonal unit cell (6 atoms) twice along each lattice vector resulting in 16 Mn, 16 Co, and 16 Ge atoms. We considered the $\text{Mn}_{1+y}\text{Co}_{1-y}\text{Ge}$ solid solution where the excess Mn, y , replaces Co on the 2c site. For the dilute limit we placed 1 Mn on the 2c-site per supercell ($y = 0.06$); in the concentrated limit 15 of the 16 2c-sites were occupied by Mn ($y = 0.94$). We note that the case of $y = 0$ and $y = 1$ correspond to MnCoGe and Mn_2Ge . The results are shown in Fig. 6.

The Mn_{2c} has little impact on the magnetic moments of either the Mn_{2a} moments or the Co or Ge moments. However Mn_{2c} does have a significant compositional dependence and is antiferromagnetically coupled to the Mn_{2a} moments. In the dilute limit, the Mn_{2c} moment $-0.6 \mu_B$ is opposite in sign but comparable in magnitude to the Co moment. The magnetic moment of Mn_{2c} reached $-1.86 \mu_B$ in the concentrated Mn_{2c} regime, which approaches the calculated value for Mn_2Ge , as expected.

We additionally performed DFT calculations for Mn

substituted on the 2d-site (Mn_{2d}). From the $2 \times 2 \times 2$ supercells, 1 of the 15 Ge atoms was replaced by Mn to give $\text{Mn}_{1.06}\text{CoGe}_{0.94}$. To examine the influence of Mn on both the 2c- and 2d-sites, we replaced 1 Co and 1 Ge atom in the supercell with Mn to give $\text{Mn}_{1.12}\text{Co}_{0.94}\text{Ge}_{0.94}$. Two different configurations of this stoichiometry were generated – one where the Mn on the 2c-site was nearest to the Mn on the 2d-site, another where it was farthest. All three configurations resulted in the same magnetic moment of $-2.9\mu_B$ for Mn on the 2d-site and an unchanged magnetic moment for Mn on both the 2a- and 2c-sites.

VI. DISCUSSION

To interpret the magnetometry measurements, we construct a simple model from the DFT determined magnetic moments. We first assume that the Mn_xCoGe compounds with $x > 1$ have the excess Mn distributed evenly between the 2c and 2d-sites. We further assume that there is disorder between the 2a and 2c site and introduce a fitting parameter, δ , which characterizes the amount of Co_{2a} defects. The distribution of elements on each site is then as follows:

$$\begin{aligned} 2a : & \text{Mn}_{(x+2)/3-\delta}\text{Co}_\delta, \\ 2c : & \text{Mn}_{(x-1)/3+\delta}\text{Co}_{1-\delta}, \\ 2d : & \text{Mn}_{(x-1)/3}\text{Ge}. \end{aligned} \quad (2)$$

In the case of Mn deficient Mn_xCoGe samples, $x < 1$, the excess Co and Ge are also assumed to be evenly distributed on the 2a-sites. When site disorder is added into the model, the elemental distribution becomes,

$$\begin{aligned} 2a : & \text{Mn}_{x-\delta}\text{Co}_{(1-x)/3+\delta}\text{Ge}_{(1-x)/3}, \\ 2c : & \text{Mn}_\delta\text{Co}_{(2+x)/3-\delta}, \\ 2d : & \text{Ge}_{(2+x)/3}. \end{aligned} \quad (3)$$

In our model, we use the experimentally determined moments, $m_{\text{Mn}_{2a}} = 2.4 \mu_B$ and $m_{\text{Co}} = 0.4 \mu_B$.¹⁰ We are not aware of any measurement of the Mn moment on the 2c-site, particularly not as a function of excess Mn. We therefore use a linear approximation to estimate compositional dependence of the Mn_{2c} magnetic moment computed from our DFT calculations. From the DFT results in Fig.6, we expect that the Mn moment on the 2c-sites in Mn_xCoGe would be approximately give by,

$$m_{\text{Mn}_{2c}}(x) = -1.43 \left(\frac{x-1}{x+2} \right) - 0.514, \quad (4)$$

in units of μ_B . Since DFT overestimates the Mn moment on the 2a-site by a factor (2.4/2.75), we rescale the above DFT prediction by the same amount. Finally, we use a constant $m_{\text{Mn}_{2d}} = -2.9$ for the Mn antisite defects on the 2d-sites, as determined from our DFT calculations.

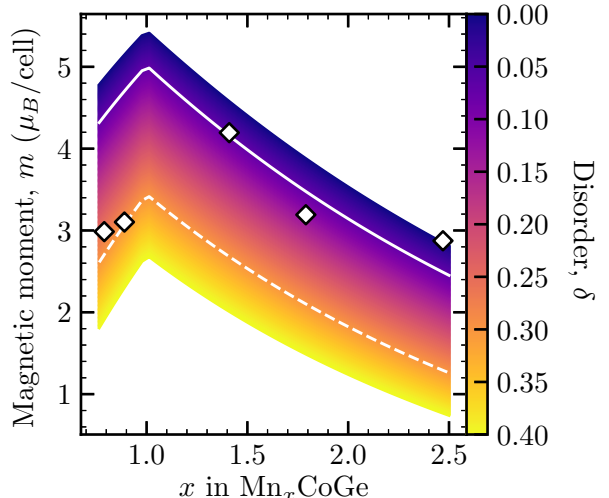


FIG. 7. The diamonds show the measured magnetic moment m per primitive unit cell of Ni_2In -type Mn_xCoGe films. The colour-plot shows the expected variation in the magnetic moment due to disorder. The solid, dashed and dash-dotted show the calculated moment for a disorder parameter $\delta = 0.07$, and 0.3 respectively with 25% vacancies on the 2c-sites.

A further refinement of the model includes 20% Co vacancies (on the 2c site), which is the maximum amount of vacancies extracted from XRD fits assuming no preferred orientation, although this was found to have a relatively small effect on the total moment per unit cell. The calculated magnetic moment as a function of x and δ is shown by the lines and colour plot in Fig. 7. The white lines show the magnetic moment per unit cell for two different levels of disorder. Below $x = 1$, the modelled moment drops with decreasing x due to a reduction in the available Mn. Above $x = 1$, the moment drops with increasing x as more Mn is forced onto the 2c-sites and 2d-sites. The colour scale reflects the decrease in magnetic moment with Co_{2a} ; a comparison with the data points allows an estimation of the disorder, δ . The disorder is as large as $\delta = 0.3$ at $x = 0.9$ and drops to $\delta = 0.07$ at $x = 2.5$. Despite informing our model with the detailed results of our DFT calculations, disorder is required to explain the ferrimagnetic behavior observed in Fig. 5 and the lower than expected magnetic moment. The absence of a compensation point in the higher Mn-content samples suggest that the alloy transitions from a Q-type ferrimagnetic (*e.g.* $\text{Y}_3\text{Ga}_{0.5}\text{Fe}_{4.5}\text{O}_{12}$) to an N-type (*e.g.* $\text{Y}_3\text{Ga}_3\text{Fe}_3\text{O}_{12}$)³¹ at larger x . Neutron scattering experiments are required to test this hypothesis.

VII. CONCLUSION

Sputtered Mn_xCoGe compounds formed a hexagonal Ni_2In -type structure over the entire compositional range

$0.8 \leq x \leq 2.5$ explored in this study. The unexpected ferrimagnetic behavior is explained by the incorporation of a fraction of the Mn onto either the 2c- or 2d-sites where DFT calculations show it couples antiferromagnetically to the 2a-sites. The possibility of changing a film from ferromagnetic to ferrimagnetic through the growth process is potentially interesting for other material systems in the context of spintronics, as the reduced moment of the ferrimagnet potentially makes it more efficient to switch with spin-transfer torque or spin-orbit torque.

VIII. ACKNOWLEDGMENTS

We would like to thank Prof. Jeff Dahn for use of the sputtering machine. We would also like to thank Andrew George and Michel Johnson for technical assistance with XRD and PPMS measurements, and finally, James Brennan and Erin Keltie for assistance in training and analysis with LA-ICP-MS measurements.

-
- * tmonches@dal.ca
- ¹ Ajaya K. Nayak, Julia Erika Fischer, Yan Sun, Binghai Yan, Julie Karel, Alexander C. Komarek, Chandra Shekhar, Nitesh Kumar, Walter Schnelle, Jürgen Kübler, Claudia Felser, and Stuart S. P. Parkin. Large anomalous hall effect driven by a nonvanishing berry curvature in the noncolinear antiferromagnet Mn_3Ge . *Sci. Adv.*, 2(4), 2016.
 - ² H. Kurt, N. Baadji, K. Rode, M. Venkatesan, P. Stamenov, S. Sanvito, and J. M. D. Coey. Magnetic and electronic properties of d022- Mn_3Ge (001) films. *Appl. Phys. Lett.*, 101(13):132410, Sep 2012.
 - ³ Yurong You, Guizhou Xu, Fang Hu, Yuanyuan Gong, Er Liu, Guo Peng, and Feng Xu. Designing magnetic compensated states in tetragonal Mn_3Ge -based heusler alloys. *J. Magn. Magn. Mater.*, 429:40–44, 2017.
 - ⁴ Jan Balluff, Jan-Michael Schmalhorst, Elke Arenholz, Markus Meinert, and Günter Reiss. Enhancing magnetic properties in Mn_3Ge thin films by doping. *Phys. Rev. B*, 97:014403, Jan 2018.
 - ⁵ O. Meshcheriakova, S. Chadov, A. K. Nayak, U. K. Röbler, J. Kübler, G. André, A. A. Tsirlin, J. Kiss, S. Hausdorf, A. Kalache, W. Schnelle, M. Nicklas, and C. Felser. Large noncollinearity and spin reorientation in the novel Mn_2RhSn heusler magnet. *Phys. Rev. Lett.*, 113:087203, Aug 2014.
 - ⁶ Ajaya K. Nayak, Vivek Kumar, Tianping Ma, Peter Werner, Eckhard Pippel, Roshnee Sahoo, Franoise Damay, Ulrich K. Röbler, Claudia Felser, and Stuart S. P. Parkin. Magnetic antiskyrmions above room temperature in tetragonal heusler materials. *Nature*, advance online publication 548:561–566, 08 2017.
 - ⁷ Sergey V. Faleev, Yari Ferrante, Jaewoo Jeong, Mahesh G. Samant, Barbara Jones, and Stuart S. P. Parkin. Origin of the tetragonal ground state of heusler compounds. *Phys. Rev. Applied*, 7:034022, Mar 2017.
 - ⁸ V. Johnson. Diffusionless orthorhombic to hexagonal transitions in ternary silicides and germanides. *Inorg. Chem.*, 14(5):1117–1120, 05 1975.
 - ⁹ S. Kaprzyk and S. Niziol. The electronic structure of comnge with the hexagonal and orthorhombic crystal structure. *J. Magn. Magn. Mater.*, 87(3):267–275, 1990.
 - ¹⁰ T. Kanomata, H. Ishigaki, K. Sato, M. Sato, T. Shinohara, F. Wagatsuma, and T. Kaneko. NMR Study of ^{55}Mn and ^{59}Co in $MnCoGe$. *J. Magn. Soc. Jpn.*, 23(1-2):418–420, 1999.
 - ¹¹ T. Kanomata, H. Ishigaki, T. Suzuki, H. Yoshida, S. Abe, and T. Kaneko. Magneto-volume effect of $MnCo_{1-x}Ge$ ($0 \leq x \leq 0.2$). *J. Magn. Magn. Mater.*, 140-144:131–132, 1995.
 - ¹² Yi-Kun Fang, Jia-Chun Yeh, Wen-Cheng Chang, Xiu-Mei Li, and Wei Li. Structures, magnetic properties, and magnetocaloric effect in $MnCo_{1-x}Ge$ ($0.02 < x < 0.2$) compounds. *J. Magn. Magn. Mater.*, 321(19):3053–3056, 2009.
 - ¹³ E. K. Liu, W. Zhu, L. Feng, J. L. Chen, W. H. Wang, G. H. Wu, H. Y. Liu, F. B. Meng, H. Z. Luo, and Y. X. Li. Vacancy-tuned paramagnetic/ferromagnetic martensitic transformation in Mn-poor $Mn_{1-x}CoGe$ alloys. *EPL*, 91(1):17003, 2010.
 - ¹⁴ Sheng-Can Ma, Dun-Hui Wang, Hai-Cheng Xuan, Ling-Jia Shen, Qing-Qi Cao, and You-Wei Du. Effects of the Mn/Co ratio on the magnetic transition and magnetocaloric properties of $Mn_{1+x}Co_{1-x}Ge$ alloys. *Chinese Physics B*, 20(8):087502, 2011.
 - ¹⁵ Qingyong Ren. *New materials for magnetic refrigeration: the magnetocaloric effect in MnCoGe-based intermetallics*. PhD thesis, The University of New South Wales, School of Physical, Environmental, and Mathematical Sciences, April 2016.
 - ¹⁶ A. Portavoce, E. Assaf, C. Alvarez, M. Bertoglio, R. Clérac, K. Hoummada, C. Alfonso, A. Charaï, O. Pilonne, K. Hahn, V. Dolocan, and S. Bertaina. Ferromagnetic mncoge thin films produced via magnetron sputtering and non-diffusive reaction. *Appl. Surf. Sci.*, 437:336–346, 2018.
 - ¹⁷ Yota Takamura, Ryosho Nakane, Hiro Munekata, and Satoshi Sugahara. Characterization of half-metallic L21-phase Co_2FeSi full-Heusler alloy thin films formed by rapid thermal annealing. *J. Appl. Phys.*, 103(7):1–4, 2008.
 - ¹⁸ W. Jeitschko. A high-temperature X-ray study of the displacive phase transition in $MnCoGe$. *Acta Crystallogr. B*, 31(4):1187–1190, Apr 1975.
 - ¹⁹ S. Kaprzyk and S. Niziol. The electronic structure of $CoMnGe$ with the hexagonal and orthorhombic crystal structure. *J. Magn. Magn. Mater.*, 87(3):267–275, jul 1990.
 - ²⁰ Konstanze R. Hahn, Elie Assaf, Alain Portavoce, Sylvain Bertaina, and Ahmed Charaï. Structural and Composition Effects on Electronic and Magnetic Properties in Thermoelectric $Mn_{1-x-y}Co_{1+x}Ge_{1+y}$ Materials. *The Journal of Physical Chemistry C*, 121(48):26575–26586, dec 2017.
 - ²¹ M. Ellner. Kristallstrukturdaten von Mn_2Ge . *J. Appl. Crystallogr.*, 13(1):99–100, 1980.
 - ²² Konstanze R. Hahn, Elie Assaf, Alain Portavoce, Sylvain Bertaina, and Ahmed Charaï. Structural and composition effects on electronic and magnetic properties in thermoelectric $Mn_{1-x-y}Co_{1+x}Ge_{1+y}$ materials. *The Journal of Physical Chemistry C*, 121(48):26575–26586, 12 2017.

- ²³ P. Hohenberg and W. Kohn. Inhomogeneous Electron Gas. *Phys. Rev.*, 136(3B):B864–B871, 1964.
- ²⁴ Walter Kohn and L. J. Sham. Self-Consistent Equations Including Exchange and Correlation Effects. *Phys. Rev. Lett.*, 140(4A):1133–1138, 1965.
- ²⁵ John P. Perdew, Kieron Burke, and Matthias Ernzerhof. Generalized Gradient Approximation Made Simple. *Phys. Rev. Lett.*, 77(18):3865–3868, 1996.
- ²⁶ G. Kresse and J. Hafner. *Ab initio* molecular dynamics for liquid metals. *Phys. Rev. B*, 47(1):558–561, 1993.
- ²⁷ G. Kresse and J. Furthmüller. Efficient iterative schemes for ab initio total-energy calculations using a plane-wave basis set. *Phys. Rev. B*, 54(16):11169–11186, 1996.
- ²⁸ G Kresse and D Joubert. From ultrasoft pseudopotentials to the projector augmented-wave method. *Phys. Rev. B*, 59(3):11–19, 1999.
- ²⁹ G Kresse and J Furthmüller. Efficiency of ab-initio total energy calculations for metals and semiconductors using a plane-wave basis set. *Comput. Mater. Sci.*, 99(1):16–29, 2007.
- ³⁰ Emmanuel Arras, Damien Caliste, Thierry Deutsch, Frédéric Lançon, and Pascal Pochet. Phase diagram, structure, and magnetic properties of the ge-mn system: A first-principles study. *Phys. Rev. B*, 83:174103, May 2011.
- ³¹ S. Chikazumi and C.D. Graham. *Physics of Ferromagnetism 2e*. International Series of Monogr. OUP Oxford, 2009.